GA–A24273

ELM PARTICLE AND ENERGY TRANSPORT IN THE SOL AND DIVERTOR OF DIII–D

by
M.E. FENSTERMACHER, A.W. LEONARD, P.B. SNYDER, J.A. BOEDO, R.J. COLCHIN, R.J. GROEBNER, D.S. GRAY, M. GROTH, E. HOLLMANN, C.J. LASNIER, T.H. OSBORNE, T.W. PETRIE, D.L. RUDAKOV, H. TAKAHASHI, J.G. WATKINS, L. ZENG, and the DIII–D TEAM

APRIL 2003

DISCLAIMER

GA–A24273

ELM PARTICLE AND ENERGY TRANSPORT IN THE SOL AND DIVERTOR OF DIII–D

by

M.E. FENSTERMACHER,* A.W. LEONARD, P.B. SNYDER, J.A. BOEDO,†
R.J. COLCHIN,‡ R.J. GROEBNER, D.S. GRAY,† M. GROTH,* E. HOLLMANN,†
C.J. LASNIER,* T.H. OSBORNE, T.W. PETRIE, D.L. RUDAKOV,†
H. TAKAHASHI,# J.G. WATKINS,Δ L. ZENG,§ and the DIII–D TEAM

This is a preprint of a paper to be submitted for publication in *Plasma Physics and Controlled Fusion.*

*Lawrence Livermore National Laboratory, Livermore, California.
†University of California, San Diego, California.
‡Oak Ridge National Laboratory, Oak Ridge, Tennessee.
#Princeton Plasma Physics Laboratory, Princeton, New Jersey.
ΔSandia National Laboratories, Albuquerque, New Mexico.
§University of California, Los Angeles, California.

Work supported by
the U.S. Department of Energy
under Contract Nos. W-7405-ENG-48, DE-AC03-99ER54463,
DE-FG03-95ER54294, DE-AC05-00OR22725, DE-AC02-76CH03073,
DE-AC04-94AL85000 and DE-FG03-01ER54615

GENERAL ATOMICS PROJECT 30033
APRIL 2003

ABSTRACT

Results from a series of dedicated experiments measuring the effect of particle and energy pulses from Type-I Edge Localized Modes (ELMs) in the DIII-D scrape-off layer (SOL) and divertor are compared with a simple model of ELM propagation in the boundary plasma. The simple model asserts that the propagation of ELM particle and energy perturbations is dominated by ion parallel convection along SOL field lines and the recovery from the ELM perturbation is determined by recycling physics. Time scales associated with the initial changes of boundary plasma parameters are expected to be on the order of the ion transit time from the outer midplane, where the ELM instability is initiated, to the divertor targets. To test the model, the ion convection velocity is changed in the experiment by varying the plasma density. At moderate to high density, n_e/n_{Gr} = 0.5-0.8, the delays in the response of the boundary plasma to the midplane ELM pulses, the density dependence of those delays and other observations are consistent with the model. However, at the lowest densities, $n_e/n_{Gr} \sim 0.35$, small delays between the responses in the two divertors, and changes in the response of the pedestal thermal energy to ELM events, indicate that additional factors including electron conduction in the SOL, the pre-ELM condition of the divertor plasma, and the ratio of ELM instability duration to SOL transit time, may be playing a role. The results show that understanding the response of the SOL and divertor plasmas to ELMs, for various pre-ELM conditions, is just as important to predicting the effect of ELM pulses on the target surfaces of future devices as is predicting the characteristics of the ELM perturbation of the core plasma.

I. INTRODUCTION

The attractiveness of a tokamak fusion reactor design involves both core plasma performance and the performance of the power and particle exhaust systems. High core performance necessarily produces large power and particle loads that must be removed from the device. In conventional tokamaks operating in high confinement mode (H-mode) with edge localized modes (ELMs) instabilities, the non-linear reconnection of the instability produces transient perturbations of the edge pedestal and thereby mechanisms for both particle and energy exhaust from the core plasma. Experimentally this can have the beneficial effect of helping to reduce the buildup of impurities in the core plasma but it also produces the detrimental effect of transient heat and particle loads on the plasma facing components (PFCs) in the device. Reactor scenarios desire an optimized solution in which the impurity exhaust aspect is maintained while the peak loads to the PFCs are minimized.

Control of the ELM perturbation and the optimization of PFC design in future tokamaks requires understanding of the ELM energy at the PFC surface (energy loss from the core plasma times the fraction that is transported to the targets), the spatial profile of the ELM particle and energy burst on PFC surfaces and the duration of the transient loads. In a 1-D approximation, ablation of candidate PFC materials can occur if, during an ELM, $Q/(At^{1/2})$ exceeds a threshold value, where Q/A is the ELM deposition energy density and t is the ELM deposition time. Therefore the ELM energy and profile effects are stronger drivers of the PFC damage than the duration. The estimate of the ablation threshold for the graphite target tiles proposed for ITER is 45 MJ $m^{-2} s^{-1/2}$ [1,2]. Scaling of results from present experiments with Type-I ELMs indicates that this threshold may be exceeded by as much as a factor 5 in ITER [2,3]. This extreme case leads to predictions of very limited divertor PFC lifetime of less than 10^4 ELM events (one full-length discharge) in ITER [2,3]. Complete physics understanding of the processes leading to ELM deposition on the material surfaces is needed to allow development of mitigation schemes that solve this problem.

Fast diagnostic measurements of ELM effects in the scrape-off-layer (SOL) and divertor of the DIII-D tokamak [4] described in this paper will be used to improve the capability of predicting ELMs in future tokamak reactors. The measurements address the magnitude of the ELM energy leaving the core plasma, the propagation of the transient ELM pulses of particles and energy in the SOL and divertors to the target surfaces, the profiles of the deposition on the target surfaces and the scaling of the deposition time. A

recent dedicated experimental campaign obtained comprehensive data from multiple diagnostics in DIII-D H-mode plasmas [5] with Type-I ELMs [6] for a range of core plasma densities. Comparison of the ELM behavior as a function of core density is the subject of this paper.

The paper is organized as follows. First a summary of DIII-D edge pedestal stability analysis pertinent to the Type-I ELM instability is given in Section II. Next a simple model of ELM particle and energy transport in the SOL and divertor is given in Section III. The fast diagnostics used on DIII-D to measure ELM effects in the pedestal, SOL and divertor are described in Section IV. Experimental results are given in Section V beginning with ELM effects at the outer midplane pedestal, then the outer midplane SOL, the remainder of the SOL and divertor legs, and finally ELM effects at the target plates. Section VI presents a discussion of the observations focussing on whether the qualitative differences in behavior at low vs high density agree with predictions of the simple model. Conclusions and requirements for future experimental and computational work are given in Section VII.

II. SUMMARY OF STABILITY THEORY FOR TYPE-I ELMs

Two assumptions are critical to the analysis in the remainder of this paper, namely that: 1) the Type-I ELM instability is poloidally localized near the outer midplane, and 2) the instability threshold is related to ideal MHD instabilities. These assumptions have been explored extensively, but no single mode produces the dependence of the threshold on control parameters seen in experiments [7-36]. Comprehensive reviews of ELM phenomena [6,7] and theory [8-10], and related reviews of pedestal physics [11-14] are available. A brief review of conclusions from the recent theoretical work and the current working model of the ELM instability in the edge pedestal are given in this section.

The proposal that ELMs were related to ideal MHD instabilities came from observed characteristics of the fluctuations prior to the ELM, the proximity of the edge pressure gradient at the ELM time to an ideal MHD limit, and the short time scale for the ELM instability growth. This was explored in numerous studies including those focussed on low toroidal mode number (low-n) current or pressure driven kink modes [15-19] and those concentrating on infinite-n ballooning modes [20,21]. However these "pure" modes were ruled out as the single cause of ELMs because their responses to variations in control parameters, for example triangularity [22] or squareness [23], did not match experiment. In addition, the pressure gradient at the nominal first stability limit for infinite-n ballooning modes was exceeded in experiments indicating that second stability regime access [24-27] may play an important role in the formation of large ELMs [22].

The emerging working model for the ELM instability at DIII-D is that it is generally an intermediate-n coupled peeling-ballooning mode [22,23,27–29]. Pure peeling modes are driven unstable by large edge currents, but are stabilized by a pressure gradient. High-n pure ballooning modes are destabilized by large pressure gradient at low edge current. These pure modes do not follow all of the experimental observations. However, coupled peeling-ballooning modes are predicted to be unstable at large pressure gradient and large edge current and this is consistent with conditions near the ELM threshold in experiments. Intermediate-n coupled peeling/ballooning modes are generally predicted to be most unstable, due to line bending and wall stabilization of low-n modes, and second stability and FLR stabilization of high-n modes [27–31]. The simplified theoretical picture [23,27,32] is summarized in magnetic shear s vs pressure gradient α space in Fig. 1. This simplified s-α calculation is shown to provide physics insight, though present

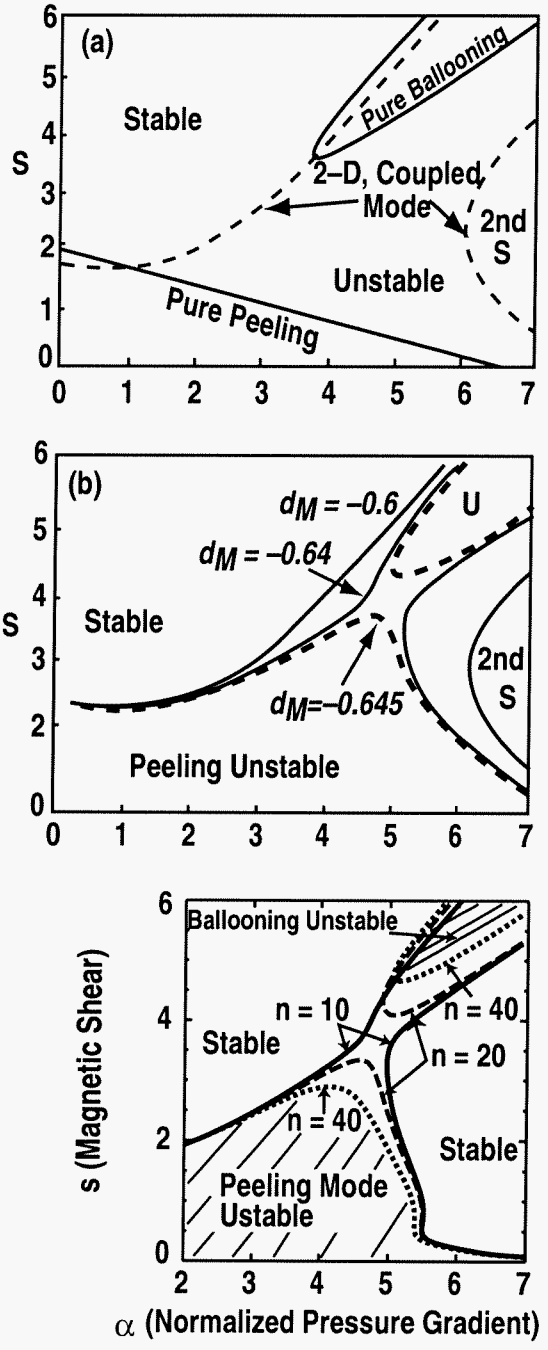

Fig. 1. Simplified ELM stability model in magnetic shear (s) vs normalized pressure gradient (α) space [27,32]. (a) Unstable regions from simple 1D calculations [28] for pure ballooning (high s, α) and pure peeling modes (low s, α), first stability regime for infinite-n ballooning (high s, low α) and second stability regime (moderate s, high α). (b) Access to second stability regime vs magnetic well parameter d_M for n = 20 coupled 2-D peeling-ballooning mode. (c) Access to second stability regime vs toroidal mode number n for $d_M = -0.645$.

calculations are done in full non-local geometry as discussed below. In these diagrams $d_M = D_M\ s^2/a$ is the "effective magnetic well depth" [32], where D_M is the Mercier coefficient [33] ($D_M < 1/4$ is the Mercier stability criterion derived for high aspect ratio circular plasmas [33]) and the factor s^2/α provides a measure of the effect of plasma shaping and aspect ratio. Poor shaping, for example low triangularity or very high or very low squareness, is predicted to destabilize the mode and this is seen in experiments [23]. For optimized shaping, access to the second stability regime is possible, with high-n modes most easily accessing second stability access [Fig. 1(b)]. Alternatively, for fixed shape, the theory predicts a minimum n-value for second regime access [n~15 in the example of Fig. 1(c)]. Second regime access theoretically allows a larger pressure gradient buildup before ELM instability onset, lower n-number of the most unstable mode, and therefore larger, lower frequency ELMs. The measured size and frequency of Type-I ELMs in DIII-D as a function of shaping is consistent with these predictions [22,23].

This theoretical picture implies that the ELM threshold should depend on: 1) edge current through the peeling instability thresholds, 2) pressure gradient through both the ballooning threshold and the bootstrap current contribution to the edge current profile, and 3) edge collisionality through the bootstrap current. These predictions are consistent with presently available pedestal measurements; they will be further tested by direct pedestal current density measurements [37] in the near future. Even at constant edge pedestal pressure, changes in the pedestal density and temperature profiles may affect the threshold because of the different dependence of the bootstrap current on density and temperature gradients. Also, since the ELM threshold depends on edge collisionality, the edge impurity content matters. Optimizing the edge for minimum ELM size and depth into the pedestal, sufficient ELM frequency for core impurity control, and maximum pedestal height at the time of the ELM for core confinement is therefore an extremely complicated goal.

The recent development of the ELITE code [27,34] has allowed efficient calculation of the actual intermediate-n peeling-ballooning stability limits in shaped, non-local geometry. This has enabled quantitative comparisons of theoretical peeling-ballooning stability limits and mode structures with ELM onset and characteristics in multiple machines [27,29,35], as well as studies of pedestal stability limit variation with shape and other equilibrium parameters [29,31,36]. Calculations indicate that the source perturbation from the pedestal into the SOL is generally expected to be dominant at the outer midplane and toroidally asymmetric [3,27,31,38]. From coupled peeling-ballooning theory the ELM size and the depth of the ELM perturbation into the pedestal may be determined by the n-number of the most unstable mode which will likely be in an intermediate range $2 < n < 40$ [27]. Toroidal asymmetry of the perturbation in the SOL

and divertors should therefore be expected. The perturbation should generally be dominant poloidally in the bad curvature region of the low-field-side midplane. Finally, detailed 2-D calculations combining accurate equilibrium reconstruction with the EFIT code [39] and linear peeling-ballooning with ELITE [34], indicate that the depth of the perturbation and therefore the ELM size should be reduced as density increases in good agreement with recent observations [3,29,38] on DIII-D. At high density the pedestal collisionality is higher and the edge bootstrap current is reduced. The steep gradient region of the pedestal pressure is also narrower at high density. Both of these effects contribute to smaller ELMS through destabilization of higher-n toroidal modes with narrower radial extent than the low-n modes that dominate the large ELMs at low density [29, 38].

III. SIMPLE MODEL OF TRANSPORT IN THE SOL AND DIVERTOR DURING AN ELM

A simple model of transport on the open field lines of the SOL and divertor during an ELM cycle, which is supported by theoretical simulations [40-43], asserts that there should be at least three distinctly different time scales on which energy and particle transport can occur, namely: 1) the electron conduction time (~ several μs), 2) the ion convection time (~ several 100 μs), and 3) the neutrals recycling time (~ several ms). In this simple model, the ELM cycle consists of a linear phase (ELM onset and build-up), a non-linear reconnection (ELM crash), and a recovery phase. The model assumes that during the build-up and the crash, particle and energy transport across the separatrix onto the open field lines of the SOL is substantially increased. The density of the particles lost from the pedestal can exceed the density in the SOL prior to ELM onset by factors of 2–4 and the temperature of the ejected particles can exceed the SOL temperature by more than a factor of 10. The spatial distribution of the perturbation is assumed to be poloidally localized near the low-field-side midplane consistent with the peeling/ballooning theory for the instability (Section II). For this simple model the toroidal distribution is assumed to be uniform and no perturbation of the pre-ELM flux surfaces and open field lines is included. The midplane perturbation contains both hot electrons and hot ions. Even at the modest temperatures of the SOL, parallel conduction of the electron energy to the targets is very fast (~1–10 μs on DIII-D) compared to any other transport mechanism. Part of the model is that the sheath potential at the targets should rise on this time scale. The temperature in the SOL also should rise and become more uniform along the field lines. The ions that existed near the targets prior to the ELM onset are assumed to fall through the elevated sheath potential and remove part of the ELM energy from the SOL. However, the majority of the ELM energy is assumed to be removed from the SOL when the ELM-expelled ions are convected from the outer midplane to the targets. Convection of ions, even at the high ion sound speed consistent with the pedestal temperature, gives an ion transit time in DIII-D of the order of 100 μs. In this model, it is the high energy pedestal ions, as they fall through the elevated sheath, that remove from the SOL the bulk of the energy lost from the pedestal. Recycling of the bulk of the ELM ions then further increases the density and hydrogenic radiation near the targets. The target perturbation relaxes, after the delivery of the ELM ejected particles, on the time scale of recycling equilibration set by neutral loss from the target region (~ several ms in DIII-D).

Additional SOL and divertor effects that may complicate the model of energy and particle transport during the ELM cycle include: secondary electron emission from

surfaces, liberation of deeply trapped neutrals by high energy ion bombardment, anomalous perpendicular transport, impurity release by high impact energy physical sputtering, and competition between the time scale of the ELM instability at the midplane and the transit time for transport to the target surfaces. The simple model assumption that the sheath potential increases substantially and the SOL temperature equilibrates can be nullified somewhat if substantial secondary electron emission occurs at the targets [40]. However, the secondary electron emission coefficient is a strong function of the target material and temperature; predictions for the graphite tiles and target temperatures in present experiments indicate that this may be a small effect [41]. Ion bombardment of the targets at the high energies obtained from the elevated sheath may penetrate far deeper into the targets than the pre-ELM impacts and release deeply trapped neutrals. If this occurred the density rise near the targets, as a result of an ELM, could exceed even the density of the particles expelled at the midplane. Particles and energy transported into the SOL during the ELM cycle can also be lost to the main chamber walls by perpendicular transport. For unperturbed magnetic field lines, typical anomalous perpendicular transport to the main chamber walls, estimated from between ELM radial profiles, would be slower (~0.5–1 ms) than parallel transport along the field lines to the targets (~100 μs). However, the ELM instability could produce anomalously high cross field transport by field line stochasticity or other mechanisms. The target heat flux width should be set by the competition between perpendicular and parallel transport in the SOL. Enhanced impurity sputtering by high energy particles lost from the pedestal during the ELM cycle, both at the targets and at surfaces in the main chamber if there is substantial perpendicular transport, must be included in a complete model of ELM effects in the SOL. Finally, the simple model implicitly assumes that the ELM instability exists at the midplane long enough for ion convection to produce enhanced particle flux at the targets. If the ELM instability ends before the expelled ions can reach the target then there may be no mechanism for removing thermal energy from the pedestal during the ELM build-up and crash. This picture would imply that one should observe ELM cycles in which particles were expelled from the pedestal but the pedestal temperature did not decrease.

The simple model above and the various additional effects are strongly dependent on the density or collisionality regime of the plasma on the open field lines. The detailed measurements presented in the Sections V and VI show significant qualitative as well as quantitative differences for different density regimes. The consistency of the observations with the model and implied needs for future work in areas where the data contradict the model are discussed in Section VII.

IV. ELM DIAGNOSTICS IN THE SOL AND DIVERTOR

Diagnostic measurements on DIII-D that are capable of sampling during Type-I ELM events provide electron density, temperature and D_α emission in the pedestal; density, temperature and potential in the midplane SOL; total radiation around the SOL; line radiation profiles in the divertor plasma; and heat flux, particle flux, surface current, D_α and impurity emission on the targets. A poloidal cross section showing the locations of these diagnostics and the plasma equilibrium shape used in these experiments, as calculated by EFIT [39], is given in Fig. 2. To compare diagnostic measurements at different toroidal locations, toroidal symmetry of the equilibrium flux surfaces is assumed and the unperturbed poloidal flux surfaces between ELMs are used. There is some experimental evidence that toroidal asymmetries are introduced during ELMs (Section V). The error introduced by perturbations of the equilibrium during ELMs is unknown at this time although active research is underway in this area [44-45]. For reference, the detailed capabilities of each of the diagnostics used in this paper will be described in this section; results from measurements during the ELM cycle are presented in Section V.

The electron density (n_e) and temperature (T_e) in the pedestal during ELMs are determined by Thomson scattering measurements and reordering of multiple measurements based on their time delay from the nearest ELM event [38]. For these experiments four of the seven lasers in the DIII-D Thomson scattering system were used to produces a profile of n_e and $\mathbf{T_e}$ in the pedestal region at an 80 Hz rate with a laser pulse duration of 50 ns. Typical ELM frequency in these experiments is 60–100 Hz. During a typical discharge with steady conditions for the 3–4 second current flattop, 240–320 Thomson radial profiles are obtained, each of which samples a different part of the ELM cycle. These profiles are re-ordered based on the time delay between the measurement and the ELM onset. The perturbation due to the ELM is then found by linearly extrapolating the data just before and just after the ELM to the time of the ELM onset [38]. This is done for all spatial locations measured by the Thomson system to generate profiles of n_e or T_e just before and just after ELMs. Spatial resolution in the pedestal region was 0.7 cm mapped to the midplane. The average pedestal temperature width was 2.5 (3.5) cm and the average density width was 4.0 (2.5) cm in the low and high density cases respectively.

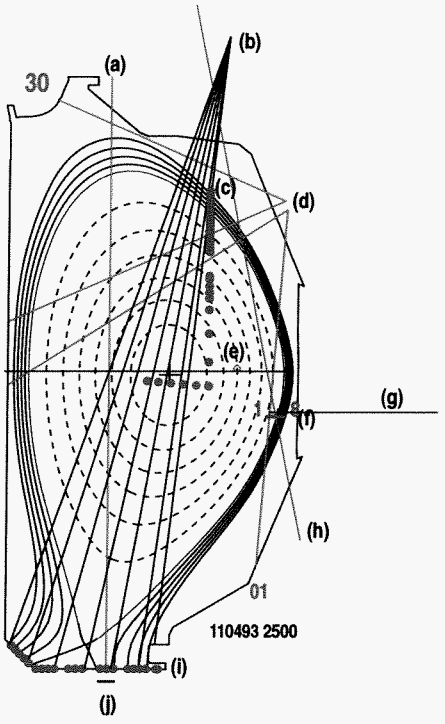

Fig. 2. Cross section of DIII-D showing typical plasma shape used in these experiments and many of the diagnostics used in the ELM analysis. Lines of sight are shown for (a) divertor interferometer, (b) divertor D_α detectors, (c) core Thomson scattering, (d) fast bolometer array, (e) pedestal ECE (f) midplane D_α detectors, (g) midplane reciprocating probe, (h) pedestal softx-ray, (i) target Langmuir probes, and (j) magnetic probe. SOL field lines shown have 1 cm separation at the outer midplane.

The outer midplane density profile in the SOL and steep gradient region of the pedestal during the ELM cycle is obtained up to a cutoff density of 1.0×10^{19} m^{-3} from reflectometry measurements [46]. Sampling rates of the density profile can be as high as 40 kHz. Spatial resolution can be as small as 0.2 cm. The profile from reflectometry agrees well with the Thomson data for various times in the ELM cycle for the density range where the diagnostics overlap. Density at the top of the pedestal was varied from 4×10^{19} m^{-3} to 1×10^{20} m^{-3} so the reflectometry profiles for this campaign cover the region from the outer SOL to just inside the separatrix (normalized radius, $\rho = 0.99$).

A reciprocating probe, plunging horizontally at 18.8 cm below the outer midplane, gives very fast data on the radial structure of density, temperature and floating potential during ELMs [47]. Sampling rates as high as 1 MHz are routinely obtained. For maximum plunging velocities of 2 m/s this implies a minimum spatial resolution of 2 μm/sample. For typical ELM frequencies of 60–100 Hz and ELM cycle duration of 1–3 ms in these experiments, the probe moves up to 2–6 mm radially during the ELM cycle and up to 2–3 cm in the time between ELMs.

The radial profile of the recycling flux during ELMs is calculated using D_α measurements from a tangentially viewing array of chords through the SOL located 20 cm below the outer midplane [48]. Acquisition rates as high as 100 kHz are achieved for eight tangential chords with a radial separation of 1.0 cm. For the typical unperturbed equilibrium used in these experiments, 2–3 of these chords are in the outer midplane SOL and 5–6 chords span the pedestal region. Abel inversion techniques are used to reconstruct a radial profile of D_α emission. The Thomson scattering measurements of n_e and T_e are then used to convert D_α emission to a radial profile of ionization flux.

A poloidal array of fast radiometer detectors measures total radiated power during ELMs along multiple chordal views in the SOL and divertor [49]. Fast AXUV photodiode detectors are used with sampling rates as high as 500 kHz. Thirty poloidal chords viewing vertically down from an upper outside port span the entire plasma. To increase the signal to noise level for SOL radiation pulse propagation analysis, the SOL is separated poloidally into 10 spatial zones. The perpendicular width of each zone is 3 cm at the outer midplane and follows a flux surface poloidally. Radiated power is assumed constant within each zone. The emission in each zone vs. time is then reconstructed, using the path length for each of the 30 chords through each of the 10 zones, by solving an over-determined matrix problem using least-squares techniques. The inversion routine is constrained to give positive emissivities only. The poloidal locations of interfaces between zones are chosen to minimize degeneracy of the solution. Since the perpendicular width of the SOL radiation profile during ELMs is not well known, a width of several cm is chosen here, which corresponds coarsely to the expected mean free path of recycled neutrals in the plasma edge region. Tests show little sensitivity of the time dependence of the radiated power to the choice of this width.

Divertor region line emission profiles during ELMs are generated in a 2-D poloidal plane from tangentially viewing, line filtered, gated-intensified camera data using tomographic reconstruction techniques [50,51]. The field rate of the cameras is 60 Hz and intensifier gate times can be a short as 0.5 μs. Narrow bandpass filters (1–3 nm) are used to select D_α (656 nm), D_γ (434 nm), CII (514.7 nm) and CIII (465 nm) line radiation during ELMs. Tomographic reconstruction techniques are used to generate 2-D poloidal profiles of emission intensity from the 3-D image data [50]. During the 3–4 second flattop of a typical discharge with nearly identical ELMs, 180–240 images are obtained. The intensifier gate times are use to relate the image times to the ELM onset time, measured at the outer midplane by the D_α array. The images are re-ordered, assuming identical ELMs, to give the evolution of the emission profile at discreet times during an ELM.

Conditions at the target surfaces during ELMs are measured with floor mounted Langmuir probes [52], a fast D_α emission array [53], tile current monitors [54], and fast IRTV [55]. Sampling rates are as high as 100 kHz for the target probes, 200 kHz for the tile current monitors and 100 kHz for the D_α array. The target probes are clustered in groups of 3–4 per tile with 2.8–3.2 cm radial separation. The tile current monitors collect the total current integrated on one of the 14×14 cm target graphite tiles. The six monitors used in this ELM study are at various toroidal locations but they are all mounted on and cover the 45 deg surface of the vessel (lower left corner of Fig. 2). The SOL flux surface that maps to 2 cm from the separatrix at the midplane intercepts the tile center in the inner divertor (Fig. 2). Seven D_α chords view the lower divertor from above with at spot diameter of 3.6 cm at the target surface. Radial profiles of target surface heat flux during ELMs were obtained at a 9 kHz rate from a fast scanning IRTV array with spatial resolution of 1.0 cm.

V. EXPERIMENTAL DATA DURING ELMs

The spatial dependence of the energy and particle transport during an ELM cycle and the variation with density were measured in a set of dedicated experiments to characterize Type-I ELMs in the boundary plasma of DIII-D. Multiple discharges were used with variation in external gas puffing to achieve a range of plasma densities in Type-I ELMing H-mode. The lower single-null (LSN) discharge shape was held essentially fixed during the flattop ELMing phases of all of the discharges in the density scan (Fig. 2). A time history of discharge parameters comparing the low and high density discharges is shown in Fig. 3. Common discharge parameters were major radius, R = 1.7 m, minor radius, a = 0.59 m, elongation, $\kappa = 1.84$, lower triangularity, $\delta = 0.55$, plasma current, $I_p = 1.4$ MA, toroidal field, $B_T = 1.75$ T, safety factor, $q_{95} = 3.5$, and injected beam power, $P_{NBI} \sim 7.0$ MW. The ion B×∇B drift direction was toward the X-point in the lower divertor. ELM data were obtained for plasmas with line-averaged density in the range $0.35 < n_e/n_{Gr} < 0.8$, where $n_{Gr} = I_p/\pi a^2$ is the Greenwald density parameter [56]. For each measurement in this paper, data from the "low density case" ($n_e/n_{Gr} \sim 0.4$) will be compared with the "high density case" ($n_e/n_{Gr} \sim 0.8$) to look for consistency of the density dependence with predictions of the simple model.

Previous experiments that varied the up/down magnetic balance near double-null (DN) divertor configurations and computational simulations of intermediate-n coupled peeling/ballooning modes in real geometry both indicate that the perturbation to the SOL by the ELM is dominant at the outer midplane. The experimental confirmation that the ELM perturbation is localized to the outboard, low-field side, of the plasma comes from a series of experiments on DIII-D that varied the up-down magnetic balance of the plasma shape [57]. The ion saturation current signals, j_{sat}, from target surface mounted Langmuir probes in both the upper and lower divertors were monitored as a function of the midplane separation of the separatrices, dR_{sep}, between the separatrices that mapped to the two X-points in the configuration. Results from the inner strikepoint probes during a dR_{sep} scan are shown in Fig. 4. ELM perturbations were seen on the j_{sat} signals from the outer strikepoints (OSP) in all configurations. For configurations magnetically biased toward either of the divertors (-0.5 cm $< dR_{sep}$ or $dR_{sep} > 0.5$ cm) the ELM perturbations to j_{sat} also appeared on inner strikepoint (ISP) probes. However, for $|dR_{sep}| < 0.5$ cm, essentially no ELM perturbations were seen on the j_{sat} signals from the ISP probes. This can only be the case if the ELM perturbation is localized to the low-field side of the plasma; if the perturbation also existed on the high-field side then it would connect on the

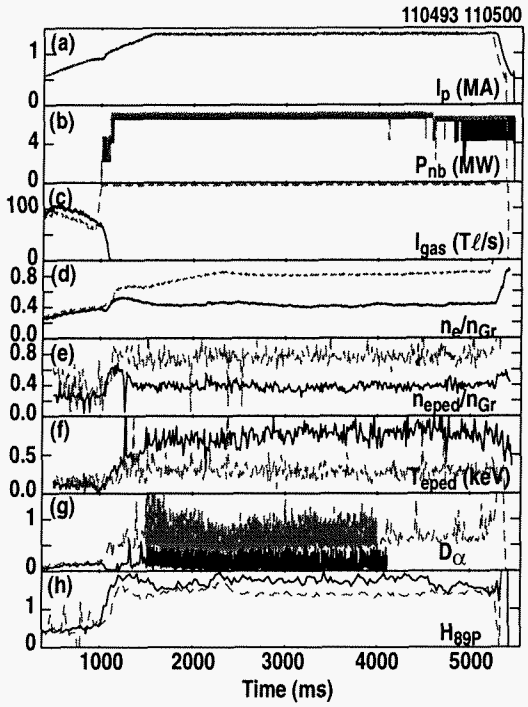

Fig. 3. Time history of the low density (solid) and high density (dashed) discharges compared in this paper, (a) plasma current, I_p (MA), (b) injected neutral beam power, P_{inj} (MW), (c) injected neutral gas, (T l/s), (d) line-averaged density normalized to Greenwald density n_{Gr}, (e) pedestal density normalized to n_{Gr}, (f) pedestal temperature (keV), (g) pedestal D_α emission at the outer midplane (10^{15} m^{-2} s^{-1} sr^{-1}), (h) core energy confinement time normalized to ITER-89P L-mode scaling [81].

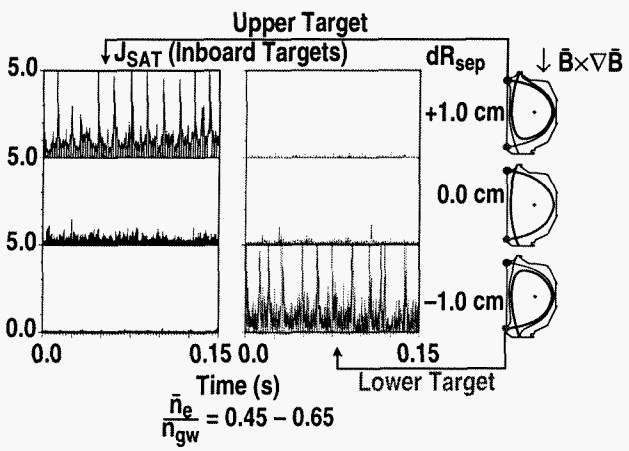

Fig. 4. Ion saturation current at the inner target as a function of up/down magnetic balance of the equilibrium. Pulses due to ELMs are seen at the inner target except in balanced double-null operation for which field lines from the outer midplane do not map to the inner target.

open field lines to the ISPs independent of dR_{sep}. This direct experimental result is predicted by linear peeling-ballooning mode simulations [27] of the ELM instability for these nearly DN configurations (Fig. 5). The amplitude of the ELM perturbation is predicted to be maximum at the outer midplane and to fall by more than a factor of 10 at the top and bottom of the plasma. Negligible ELM amplitude is predicted for the high-field side of the plasma.

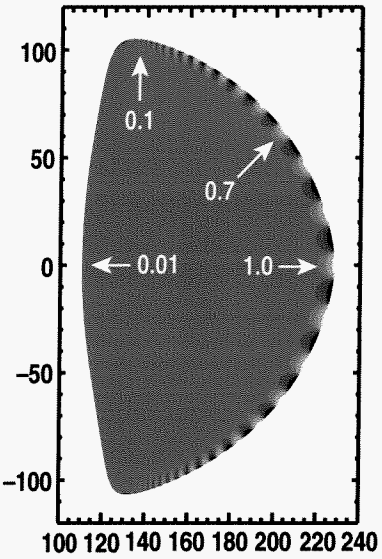

Fig. 5. Linear 2-D peeling-ballooning stability results from the ELITE code for nearly balanced DIII-D DN equilibria showing poloidal mode structure of the n=10 toroidal mode. Mode amplitude normalized to that at the outer midplane is shown at several poloidal locations.

A. Low-Field-Side Midplane Effects

Thomson scattering measurements in the edge pedestal indicate that the ELM instability reduced the edge density for all regimes of core density but the edge temperature was reduced by the ELM only in the low density regimes. Reconstructions of the pedestal and near SOL density profiles just before and just after an ELM were done using the reordering technique [38] described in Section IV. The effect of plasma density regime was obtained by comparing profiles from different discharges. Perturbations to the pedestal and SOL n_e and T_e by ELMs in plasmas with density at 40% and 80% of the Greenwald limit are shown in Fig. 6. A clear reduction of the pedestal density is seen in both cases. However, at high density there is very little change to the pedestal temperature observed. The increase in the SOL density in both cases is comparable to the decrease in the pedestal density but the observed change to the SOL temperature is a very small fraction of the perturbation to the pedestal temperature. It should be noted that the Type-I ELMs in the high density case were smaller amplitude and had higher frequency than in the low density discharges (these have been described as minimum energy ELMs by Loarte [59]).

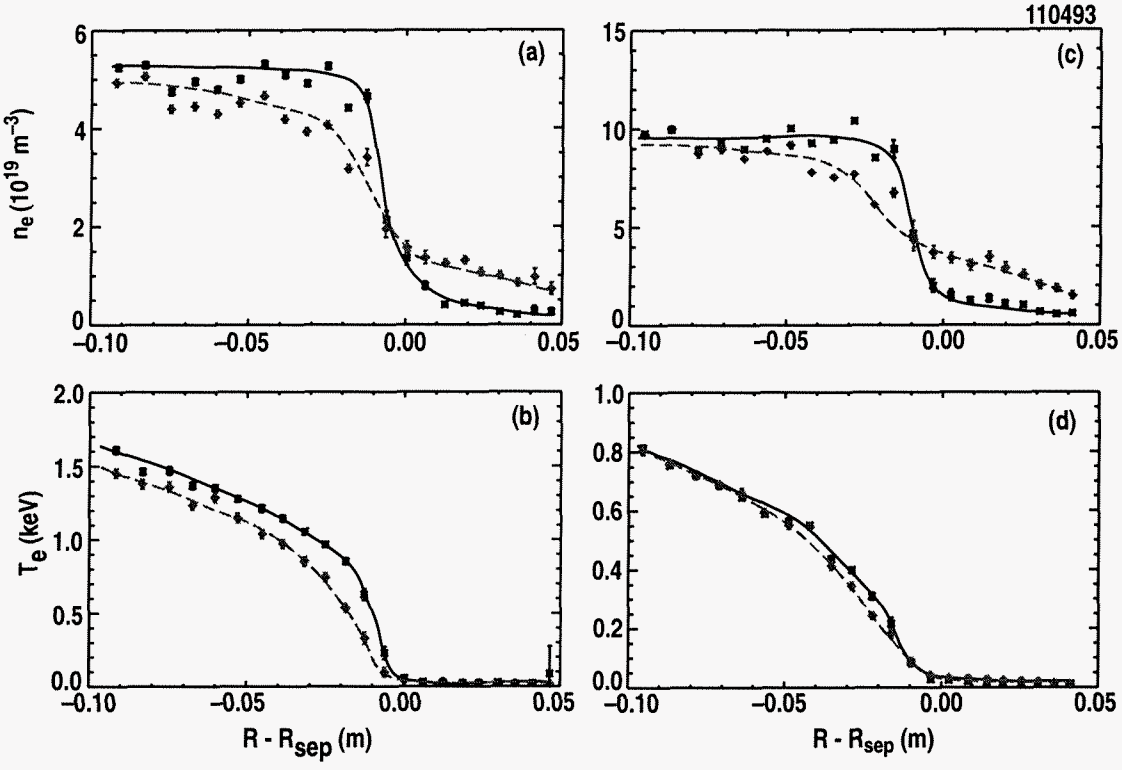

Fig. 6. Pedestal and SOL profiles of electron density (10^{19} m^{-3}) (a,c) and temperature (keV) (b,d) from Thomson scattering vs midplane radial distance from the separatrix. Profiles shown in the low density case (a,b) and high density case, (c,d). Profiles just before (solid) and just after (dashed) ELM event obtained by extrapolation to the ELM time from Thomson samples of many similar ELMs at various times relative to the ELM time.

Edge reflectometry data indicate that the ELM density perturbation propagates radially into the far SOL and the velocity is comparable to the radial propagation of other intermittent density structures in standard ohmic and L-mode plasmas [60–63]. The time evolution of the SOL density profiles from the reflectometry data is compared for the low and high density cases in Fig. 7. This data, obtained at 2 kHz sampling rate, show that in both cases the density at the radius of the outer poloidal limiter rises at the ELM onset by more than a factor of 10 to $>5\times10^{18}$ m^{-3} in one 500 μs sampling time. Data obtained in a subsequent discharge, at intermediate density, with 40 kHz sampling of the reflectometer (Fig. 8), show that the radial velocity estimated from the evolution of these profiles compares very well with the $v_r = E_\theta \times B/B^2$ velocity, where E_θ is measured by the midplane reciprocating probe. This velocity is also comparable to $E_\theta \times B$ radial velocities in the outer midplane SOL computed for intermittent density structures in L-mode plasmas [62, 63].

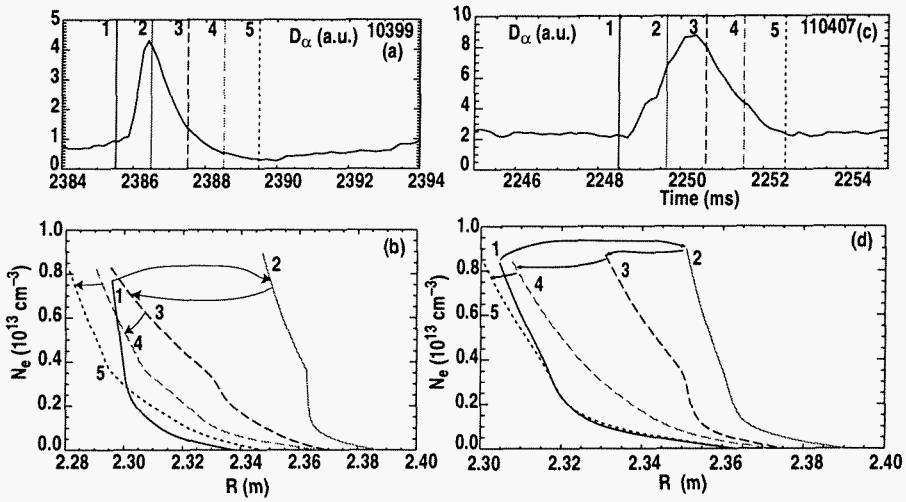

Fig. 7. ELM evolution represented by midplane D_α emission (a,c) and SOL density profiles (b,d) vs. midplane radius from the fast midplane reflectometer at several times during the ELM cycle. Profiles are at the times corresponding to the vertical lines on D_α emission history with the same linestyle. Profiles and evolution are shown in the low density (a,b) and high density (c,d) cases. Midplane separatrix is at R = 2.29 m and the poloidal limiter surface is at R = 2.365 m. Reflectometer horns are recessed between outer poloidal limiters.

Comparison of time history data from multiple point measurements indicates that, in the low density case, particle loss from the pedestal may occur before the thermal energy is expelled. This observation is similar to the ELM precursors in the SOL reported from JT60-U [64] and TCV [65]. Indirect evidence of a time delay between the effects of particle loss from the pedestal and the drop in pedestal temperature comes from comparison of "average ELM" behavior on fast magnetics, soft x-ray and D_α recycling diagnostics (Fig. 9). Here the "average ELM" behavior is obtained from a simple "coherent averaging" technique similar to that used in Refs. [64–66]. ELM times are chosen as the times of peak emission from the midplane D_α signal for a flattop period of the discharge with steady reproducible ELMs. Data in a ±5 ms window from other diagnostics are aligned to these multiple ELM times and averaged to produce the "average ELM" evolution. In the low density case, fast magnetic probe data from the divertor region and D_α emission data from the outer midplane show substantial increases at the beginning of the ELM cycle. During this time the soft x-ray and ECE signals from the edge of the core plasma change only slightly. This indicates that the instability amplitude is increasing and particles are being expelled from the pedestal and they are recycling during this early phase without any corresponding change in the pedestal temperature. The rapid drop in T_e^{ped} is indicated by the rapid decrease in the soft x-ray and ECE signals. This is likely an indication of the reconnection event at the ELM crash. The magnetics signal inverts and there is a rapid rise observed in the midplane D_α emission. The time delay between the increase in the magnetics and D_α emission vs the

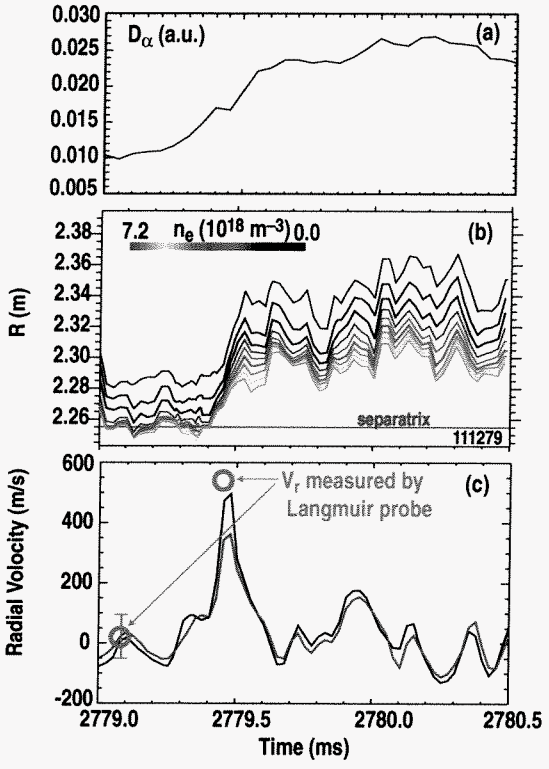

Fig. 8. ELM measured by high acquisition rate (40 kHz) reflectometer from a discharge similar to the low density case. (a) midplane D_α emission, (b) midplane radius of various density surfaces in the SOL (coded by color) with separatrix at R = 2.258 m, and (c) inferred radial propagation velocity vs time during an ELM. In (c) radial propagation velocity is shown for the $n_e = 2\times10^{18}$ m^{-3} (black) and 5×10^{18} m^{-3} (red) surfaces and compared with computed $E_\theta\times B/B^2$ radial velocity from midplane reciprocating probe measurements (green circles).

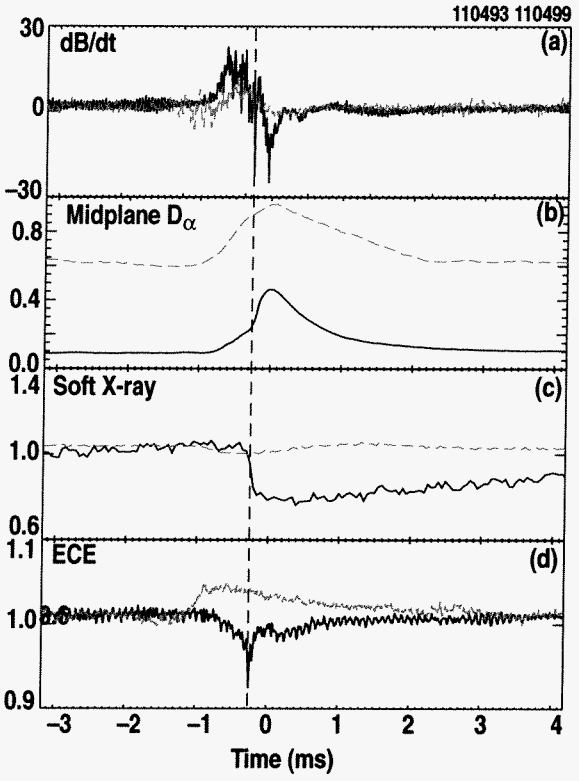

Fig. 9. Time histories of (a) divertor magnetic field variation (T/s), (b) midplane D_α emission in the pedestal (10^{14} m^{-3} s^{-1} sr^{-1}), (c) soft x-ray signal (a.u.) from a chord through the pedestal region, and (d) ECE emission from the top of the pedestal at the midplane. Traces are averaged over approximately 15 ELMs in low density (solid) and high density (dashed) discharges and plotted vs. time from the peak of the midplane D_α signal. Time of the pedestal thermal energy drop in the low density case marked by the vertical line.

inferred drop in T_e^{ped} is approximately 500 μs for this discharge. In the high density case there is essentially no T_e^{ped} reduction by the ELM and no corresponding delay between particle loss and energy loss effects can be seen. Understanding the physics mechanism behind the qualitative difference in the response of T_e^{ped} to the ELM instability may provide the key to control of the energy released from the pedestal by ELMs.

The pedestal density loss is replenished by significant ionization inside the location of the unperturbed separatrix on a recycling time scale after the ELM losses. Profiles of the volumetric ionization rate at the outboard midplane for the low and high density cases are compared in Fig. 10. Even prior to the ELM onset the maximum of the radial ionization profile is inside the separatrix (R = 225.6 cm) near the top of the pedestal. The neutrals

that fuel the edge plasma at this radius have achieved energies corresponding to the local ion temperature by multiple charge-exchange events [68]. At the ELM onset the ionization rate increases across the profile. The largest percentage change is in the SOL but the largest absolute change in the fueling rate is in the pedestal (R = 224.7 cm). The recovery times for the ionization rate after the ELM are approximately 1 ms and 3–4 ms in the low and high density cases, respectively. Integrating the total ionizations during the ELM cycle, assuming toroidal symmetry and a uniform rate in a 5 cm wide poloidal annulus, gives approximately 40% of the particle loss measured during the ELM by Thomson scattering for the low density case. This indicates that there could be factor of ~2 poloidal or toroidal asymmetries in the refueling profile at low density. At high density the ionization integral, again assuming toroidally and poloidally uniform source, indicates sufficient source to completely refuel the pedestal density loss. This may be the result of measuring a different part of an asymmetric profile in this case, but it could be consistent with a conclusion that the asymmetries in the source were reduced compared with the low density case.

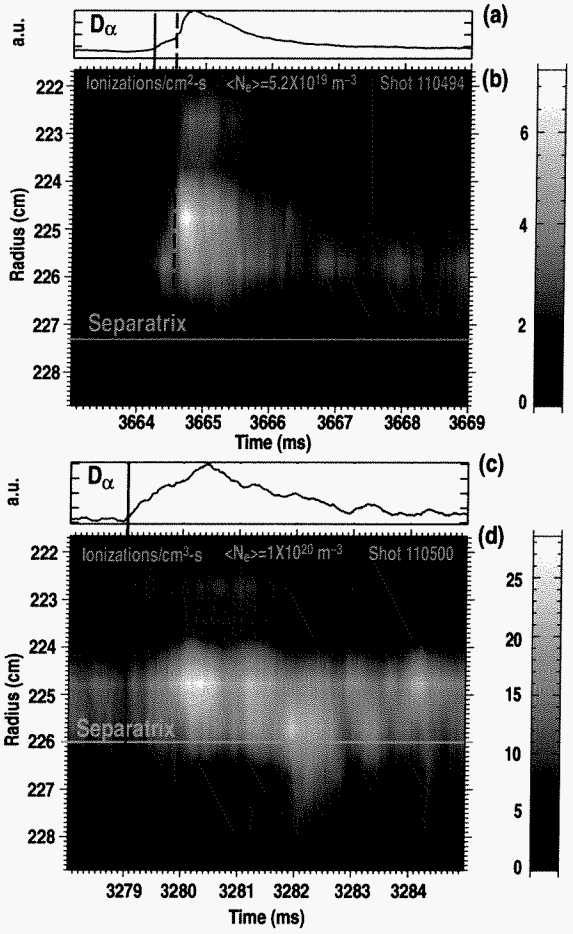

Fig. 10. Time histories of D_α emission (a.u.) from a single midplane tangential chord (a,c) and inferred profile of ionization rate (10^{15} cm^{-3} s^{-1}) across the pedestal and SOL (b,d) computed from the eight midplane D_α chords and Thomson scattering density and temperature measurements for the low density (a,b) and high density (c,d) cases. ELM onset (solid) and Δt_e^* (dashed) times shown by vertical lines.

Significant radial structure of the ELM density perturbation was inferred from measurements by the midplane reciprocating probe: the amplitude of the perturbation decreased as it propagated radially indicating spreading along the SOL field lines [61,63]. The density data from the midplane reciprocating probe for three successive ELMs are shown in Fig. 11. The midplane D_α signatures of these ELMs were nearly identical. The maximum density at the start of the ELM decreased by a factor of 3 between the measurements at 0.4 cm and 3.6 cm from the separatrix. Also the duration of

the perturbation seen on the probe increased with the radius of the measurement. The $E_\theta \times B$ radial velocity of these perturbations is estimated to be about 400 m/s near the separatrix dropping to near 100 m/s in the far SOL [61]. The probe plunge velocity is about 2 m/s over most of the plunge so the motion of the probe can be neglected compared with the propagation of the density perturbations. If the density perturbation were toroidally stationary then the evolution shown in Fig. 11 would translate directly into radial structure of the perturbation. However, there is evidence suggesting toroidal rotation of the ELM structure [61], so the evolution in Fig. 11 may show a convolution of the toroidal and radial structure of the perturbation. Future measurements at multiple toroidal locations will be needed to determine the necessary deconvolution. These observations are consistent with both perpendicular and parallel spreading of the perturbation as it propagates radially. Large variations at high frequency were also seen in the signal level indicating fine scale spatial structure in the perturbation as it moved past the probe. This fast data may contain important information for a more sophisticated model of the enhanced radial transport during the ELM but detailed analysis is just starting [61].

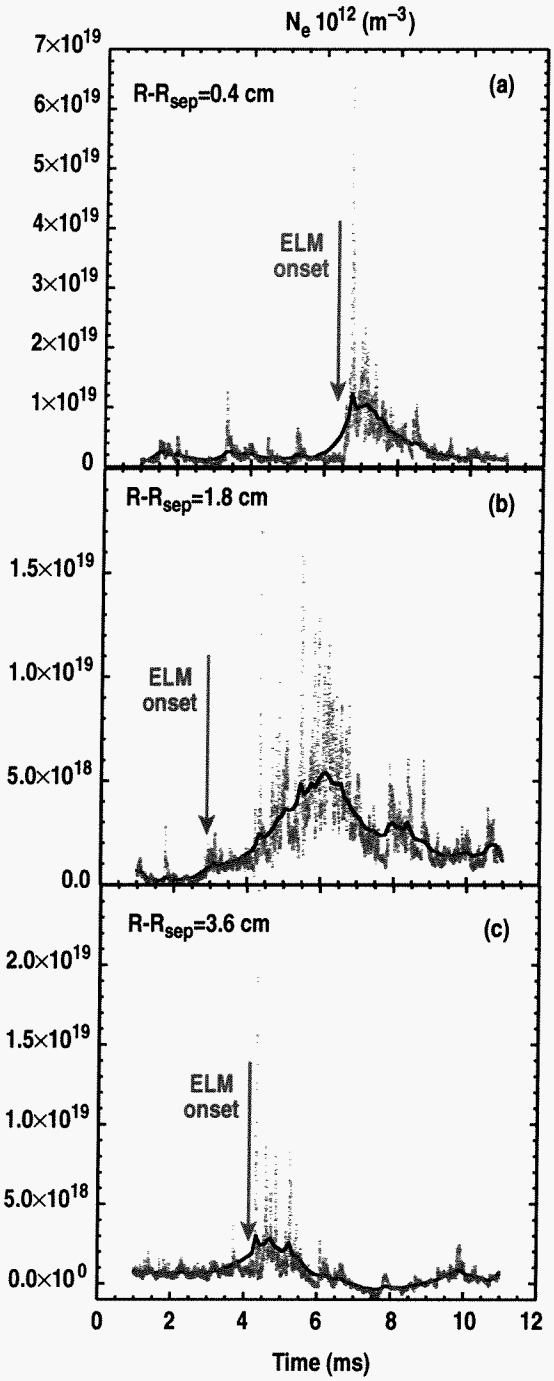

Fig. 11. Time history of density perturbation due to ELMs measured by the midplane reciprocating probe in the (a) near, (b) intermediate, and (c) far SOL for the low density case. Data from 1 MHz sampling shown in red with average shown in blue. Time scale shown allows relative comparisons but it is not correlated with any particular timing fiducial relative to the ELM evolution; vertical scales optimized for data display. Approximate time of ELM onset within data sample is indicated.

B. Poloidal SOL and Divertor Leg Effects

At high density, the timing of the ELM induced radiation perturbation due to ELMs at various poloidal locations in the SOL, calculated from the fast bolometry data, is consistent with ion convection parallel to SOL field lines from the midplane to the targets, but inconsistencies in the relative arrival times of the pulses in the two divertors are observed at low density (Fig. 12). The chordal geometry of the fast bolometer diagnostic and the averaging zones used in the analysis presented here are shown in Fig. 12(a). On the low field side of the plasma in the high density case [Fig. 12(c)] the radiation clearly peaks first in the outer SOL and then in the outer divertor consistent with propagation from the outer midplane to the outer target. Correspondingly on the high field side the radiation peaks first in the inner SOL and then in the inner divertor. The radiation peak in the inner divertor is delayed by ~120 μs compared with the peak in the outer divertor, qualitatively consistent with the longer distance along SOL field lines from the outer midplane to the inner target. In the low density case [Fig. 12(b)] somewhat different behavior is observed. The radiation peak in the outer SOL still occurs before the peak in the outer divertor. Similarly the inner SOL peaks before the inner divertor. Also the outer SOL radiation peak occurs before the inner SOL peak. These three observations are consistent with SOL parallel ion convection from the outer midplane. However, the outer divertor peak occurs after the inner divertor peak. This apparent inconsistency with simple parallel propagation of the ELM radiation pulse from the outer midplane to the two targets may indicate that local

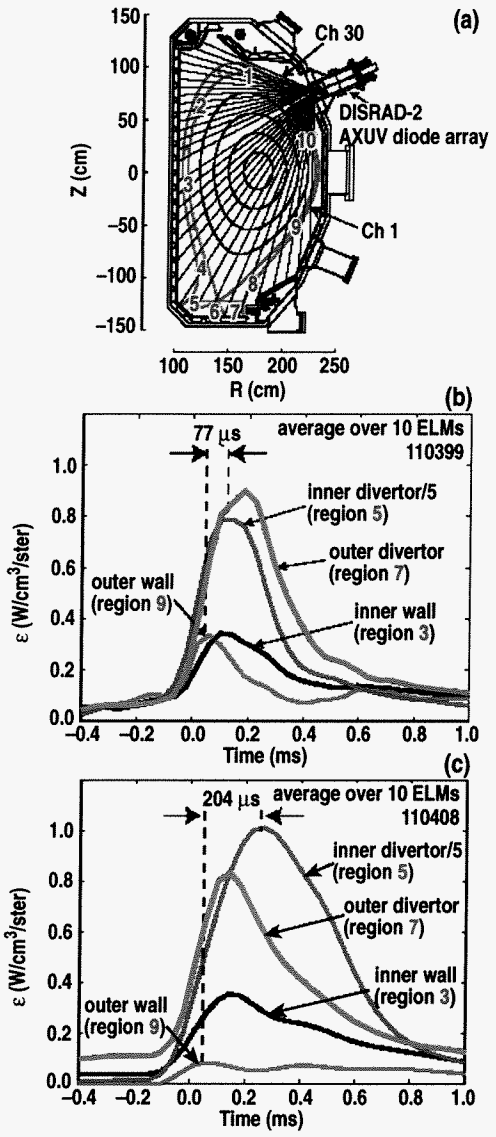

Fig. 12. SOL poloidal propagation of ELM radiation pulse from fast bolometer analysis. (a) Cross section showing chords of fast bolometer and poloidal zones used in the analysis. Time histories of radiated power density (W cm^{-2} sr^{-1}) averaged over 10 ELMs vs time from ELM onset for poloidal zones in the SOL above X-point and near the targets of the inner and outer divertors in the low density (b) and high density (c) cases.

effects at the inner target were playing a role in this low density case. One hypothesis is that for the cold, dense inner divertor before the ELM, a significant change in radiating charge states and total radiation could occur, on the much faster time scale of electron conduction, due to even minor re-heating of the plasma near the targets. Indications of divertor response to ELMs on the electron conduction time scale have been seen in JT60-U [64].

Line radiation measurements during ELMs in the divertor indicate that the ELM perturbation burns through the partially detached inner divertor at low density and it burns through the detached outer divertor leg at high density [69]. The effect of ELM perturbations on the 2-D distribution of line radiation in the divertor is shown for two different densities in Figs. 13 and 14. The distribution of CIII emission shows the location of regions with T_e ~ 6–8 eV [70]. In the low density case (Fig. 13) the dominant CIII emission prior to the ELM is upstream in the inner divertor leg SOL near the X-point. The effect of the ELM perturbation is to move the region of CIII emission down to near the ISP. In the outer divertor leg the effect of the ELM is to increase the CIII

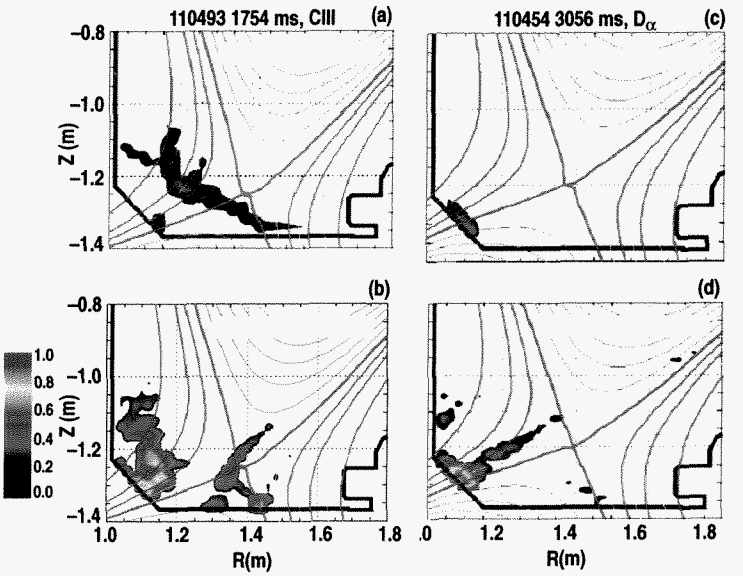

Fig. 13. Reconstructions of 2-D 465 nm CIII (a,b) and D_α (c,d) emission profiles before (a,c) and during (b,d) an ELM cycle in the low density case from the fast gated, intensified cameras. Image (b) occurs 120 μs later in the ELM cycle than image (a) and image (d) occurs 80 μs later in the ELM cycle than image (c).

emission near the target. There may have been some contribution to these changes in the emission profile from changes in the carbon source during the ELM. However, the change in the location of the peak emission strongly indicates that the inner divertor plasma temperature near the target increased as a result of the ELM pulse. The D_α

emission profile, obtained on a similar discharge, showed a factor of 3 increase in the emission near the ISP for the first image obtained after an ELM, but little overall change in the spatial profile of the emission. This is consistent with a re-heating of the ISP area although it strongly suggests an increase in the local density as well. Finally, at high density (Fig. 14) the localized distribution of CIII emission near the X-point prior to the ELM is characteristic of partially detached divertor (PDD) operation in DIII-D [70–73] in which the outer divertor leg temperature is below 2 eV. After the ELM onset, the CIII emission peaks appeared near the OSP indicating re-heating of the plasma near the outer target to the 6–8 eV range. The inner leg plasma does not re-heat in this case as it did in the low density case. Finally, the distribution of the emission returns to the pre-ELM profile on a long time scale (several ms) [69].

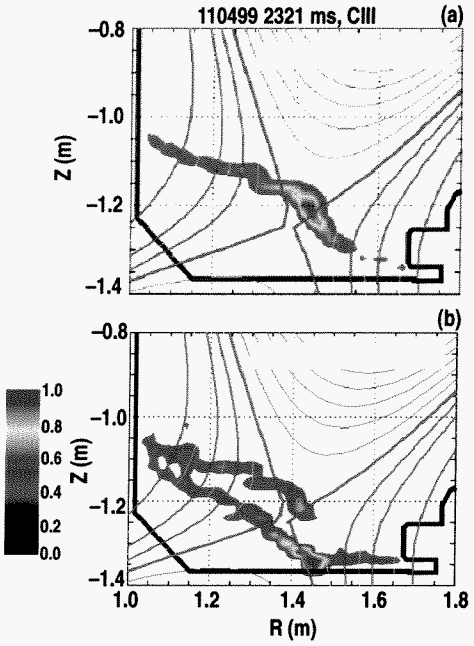

Fig. 14. Reconstructions of 2-D 465 nm CIII emission profiles before (a) and during (b) ELM cycle in the high density case. Image (b) occurs 120 μs later in the ELM cycle than image (a).

C. Divertor Target Surface Effects

The fast tile current data from the ring of toroidally spaced tiles on the 45 deg surface near the inner divertor strikepoint show significant toroidal asymmetry during ELMs and time evolution that is a function of the density regime [54]. This is the only fast SOL ELM diagnostic on DIII-D with toroidal resolution. These recent observations at high time resolution are consistent with previous measurements [74]. Time histories of a single ELM event are shown in Fig. 15 for the low and high density cases. Positive signal corresponds to net ion current flowing into the tile from the plasma. Here the net current is simply the current density profile integrated over the area of a single tile. At low density the net current flowed into the tiles during the buildup to the ELM crash and the signals showed significant temporal and spatial structure [Fig. 15(a)]. Toroidal mode analysis, limited to $n \leq 3$ by the six available tiles, showed substantial n=1, 2, and 3 amplitude [Fig. 15(b)]. The peak in the higher order mode amplitudes occurred about 7600 μs after the ELM onset. Asymmetry persisted substantially into the recovery phase, more than 1 ms after the ELM onset. At high density, the initial response to the ELM was

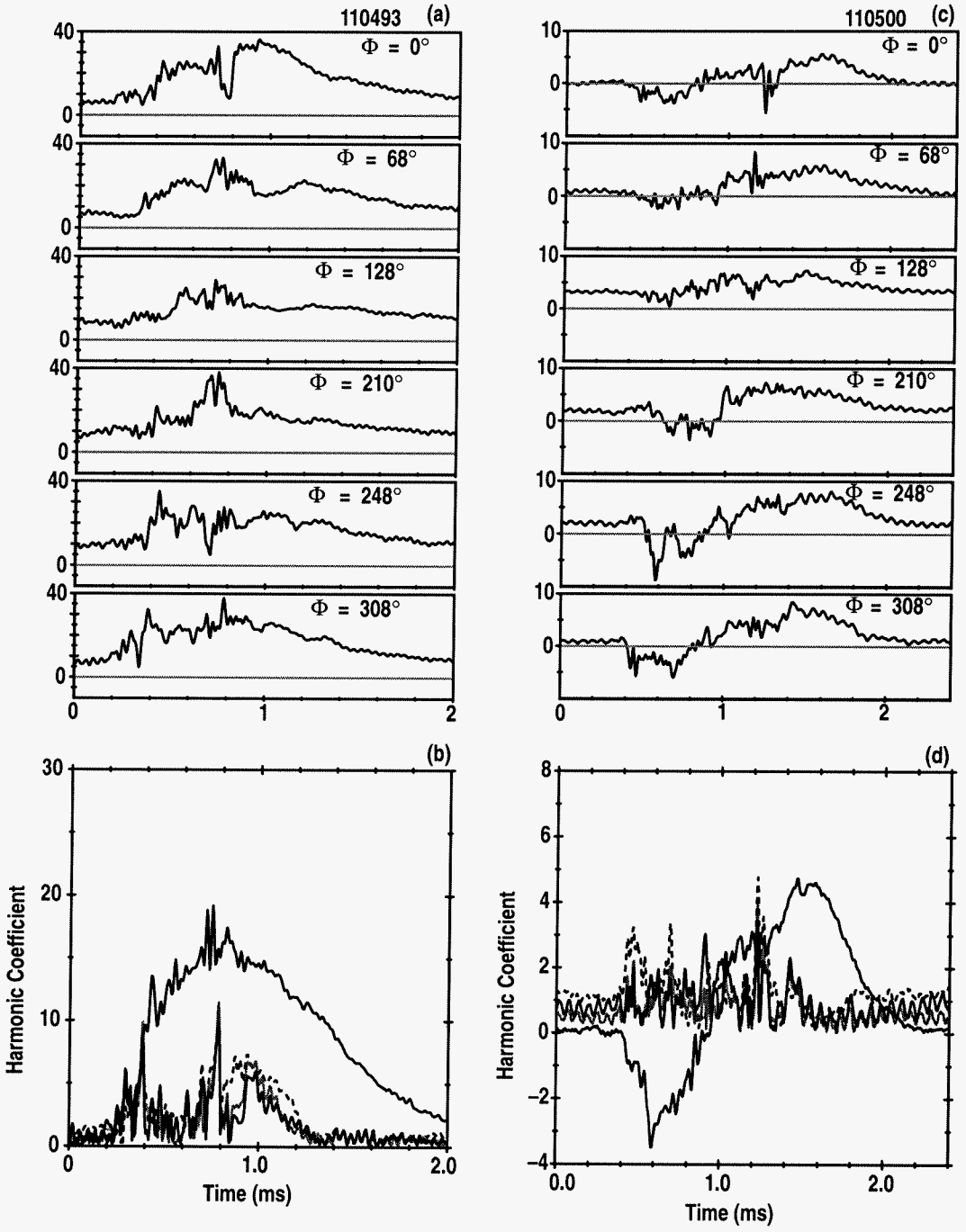

Fig. 15. Time histories (a,c) during an ELM of currents flowing from toroidally separated tiles at a radius near the ISP and the inferred toroidal mode number spectrum (b,d) in the low (a,b) and high (c,d) cases. Positive value indicates ion current flow from plasma to tile. Toroidal angle of each tile is shown. Phase and amplitude shown for the n = 0 (average of signals) trace (black). Modulus only shown for n = 1 (dashed), 2 (grey), and 3 (black) modes.

for net current to flow from the tile to the plasma, *i.e.*, opposite polarity compared with the low density case. Subsequently the net current flowed into the tile and its magnitude increased until the ELM crash. The mode number spectrum showed contributions from higher order modes similar to the low density case although the buildup phase was longer (1100 μs compared with 700 μs) and the recovery phase was dominated by symmetric perturbation (n = 0). Note that the radial profile of the SOL currents during ELMs could be bipolar over the 14 cm radial width of a tile monitor. The change in polarity of the net response with density variation could be an indication that the fine scale radial current distribution changes with density or that the strikepoints move radially [44] perhaps in a different way at different densities. However, another possible interpretation is that the initial response of the tile currents at high density shows the arrival of ELM expelled electrons and the change in polarity then signals the arrival of ELM ejected ions. At low density this signature could be masked by the fact that the inner target plasma re-heats in response to the ELM, greatly increasing the local recycling ion flux at the target. This is an active area of research [54].

The profiles of energy density deposited on the targets during ELMs show peak in/out asymmetry ratios greater than 2 and a strong decrease in energy density at the outer-strikepoint as plasma density increases. Energy deposition profiles [69,75] are obtained by integrating target heat flux measurements from the IRTV over the duration of many ELMs and averaging. Profiles from ELMs in the low, high and an intermediate density plasma are shown in Fig. 16 [75]. At the outer divertor the width of the profile is less than a factor of 2 broader than the between-ELM width as observed in other experiments [76]. At the inner divertor the profile is comparable or slightly narrower than the between-ELM width. At low density the in/out ratio of the peak energy density is ~1.5, rising to ~2.5 at intermediate density and to more than a factor of 10 at high density. The rise in this ratio is due primarily to the sharp drop in measured peak ELM heat flux at the outer target at high density. In contrast, the integrated energy under the profile is dominated by the outer target except at very high density because the width of the profile is larger near the OSP due to larger flux expansion on the outboard compared with the inboard divertor. A diagnostic issue with IR heat flux measurements, involving different temperature response of various surface materials, has been proposed in other

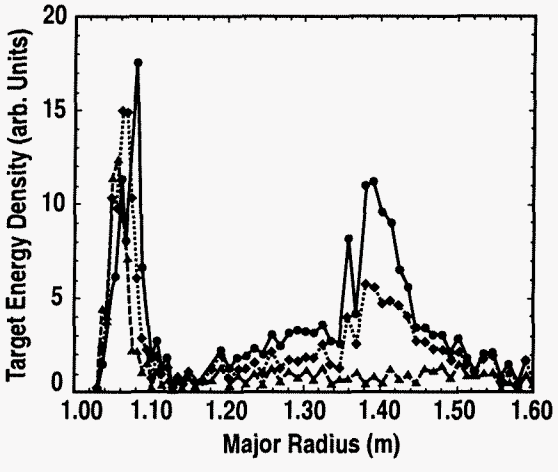

Fig. 16. Target surface energy deposition (a.u.) during an ELM (averaged over several ELMs) vs major radius for the low (solid), high (dashed) and an intermediate (dotted) density discharge.

experiments to explain large heat flux asymmetries [3,77,78]. However, in our case the asymmetry depends strongly on density so differences in target surface characteristics alone can not be the cause of the asymmetry variation. The density dependence strongly suggests that the pre-ELM condition of the divertor plasma, in particular the degree of detachment of the outer divertor leg and the neutral density that must be ionized in front of the target, plays an important role in the ELM heat flux profile in our discharges.

The time delay of inner vs. outer target surface D_α emission (recycling flux) is consistent with ion convection dominating the ELM transport, except at the lowest densities used in the experiments where very little delay is observed. The time delay between two fast D_α emission channels is obtained with a cross correlation technique. A 10 ms time window is centered on each ELM during a discharge. Within each window a cross correlation of two D_α emission signals is performed to calculate the relative delay of one signal with respect to the other for that single ELM. Each ELM is taken as distinct event and the delay values are collected as a function of the line-averaged plasma line-averaged density at the time of the ELM onset. Delay data from an inner and an outer D_α chord for all of the density-scan discharges in the campaign are shown in Fig. 17. Here the delay time is normalized to a parallel transit time, $t_{transit} = \Delta L_c / C_s\left(T_e^{ped}\right)$ where $\Delta L_c = L_c^{in} - L_c^{out}$, $L_c^{in(out)}$ are the connection lengths between the outer midplane and the ISP (OSP) along the SOL field line connecting the locations of the D_α view spots on the targets, and $C_s\left(T_e^{ped}\right)$ is the ion sound speed evaluated at the pedestal electron temperature before the ELM onset. The data shows a nearly constant normalized delay time at moderate to high density, albeit with increasing scatter as the density decreases. This is consistent with the simple model of ion parallel convection dominating the propagation of ELM perturbations in the SOL. However, at the lowest densities obtained so far in the campaign, $ne/n_{Gr} \sim 0.35$, the number of ELMs with finite normalized delay time decreased sharply and the number of ELMs with very small delay time increased. This again may be an indication of local effects at the divertor targets playing a more important role at very low densities.

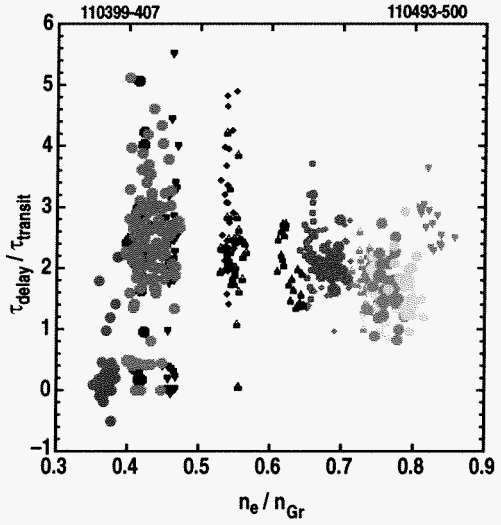

Fig. 17. Normalized delay of D_α response to ELMs in the far SOL of the inner vs outer divertor targets as a function of normalized line averaged density. Data from a single discharge are shown with the same symbol/color. Delay time is normalized to the difference in ion convection times from the outer midplane to the divertors. Density is normalized to the Greenwald density limit.

VI. DISCUSSION

The ensemble of data presented above makes two important points about ELM effects in the SOL and divertor: 1) there is good agreement between many experimental observations and the model but some inconsistencies exist even within individual diagnostic measurements and in several cases the comparison between multiple diagnostics identifies important issues, and 2) the response of the divertor to ELMs depends strongly on the density regime and pre-ELM conditions of the divertor plasma. The latter point implies that the solution for mitigating the damaging effect of ELMs on target surfaces will depend on control of the divertor conditions, in addition to control of the perturbation characteristics at the pedestal. The inconsistencies between observation and model are discussed below as are the dependencies of divertor response on divertor conditions between ELMs. The overall status of the comparison with the model, including areas of agreement and disagreement, is given in Section VII (see also Table 1) and a summary of future work needed to resolve the inconsistencies is also presented.

Local measurements at the midplane show substantial increases in far SOL density but no corresponding increases in far SOL temperature even in the low-density case for which the pedestal temperature drops significantly during ELMs. Both the reflectometry profiles and the reconstruction of the density profiles during ELMs from Thomson scattering measurements indicate that the density in the far SOL (~5 cm or ~3 times the density profile radial width between ELMs) is substantially increased during ELMs. The Thomson data in the low density case show an increase in absolute density of 5×10^{18} m^{-3} during an ELM at 4.5 cm in the SOL. This represents a factor of 2.5 increase over the between ELM density in the far SOL. Similarly the reflectometer data confirm large percentage increases in the outer SOL density at the midplane and show that even at the bumper limiter radius, 6.5 cm from the separatrix, the density rises to the 1×10^{18} m^{-3} range during an ELM. Similar increases are seen far out in the midplane SOL in the high density case. On the other hand, the Thomson data show no substantial temperature rise in the far SOL even in the low density case for which the pedestal temperature drops by 100–200 eV. The far SOL temperature data has substantial scatter but the reconstruction shows that it is ~15 eV between ELMs and no more than 25–30 eV during an ELM. However, no Thomson data within a window of ±50 μs about the ELM time exists in our dataset, so it may be that the large increases in SOL temperature expected from the drop in pedestal temperature exist for a time short compared with this window. This would imply an energy transport mechanism, at least for the electron channel, that is faster than

Table I
Summary of Simple Model Physics Mechanisms vs. Observations With Consistency Indicated in Bold Type

Physics Mechanism in the Simple Model	Available Measurement During ELM	Result During ELM at Low Density	Result During ELM at High Density
Elevated sheath should raise T_e^{SOL} throughout SOL	Midplane Δn_e^{ped}, ΔT_e^{ped}, Δn_e^{SOL}, ΔT_e^{SOL}	n_e^{ped} and T_e^{ped} both drop, n_e^{SOL} increases, no change in T_e^{SOL}	**n_e^{ped} drops, no change in T_e^{ped}, n_e^{SOL} increases, no change in T_e^{SOL}**
T_e^{ped} loss only after instability exists for ion transit time	Instability on magnetic vs. soft x-ray and ECE	**Delay of T_e^{ped} drop consistent with ion transit time**	**$\Delta T_e^{ped} \sim 0$ may be consistent with fixed instability duration and long ion transit time**
Ion convective energy transport implies n_e^{SOL} and target heat flux widths should be consistent with flux expansion, independent of density	Comparison of midplane density and target heat flux profiles	n_e^{SOL} increases farther out than outer target heat flux	n_e^{SOL} increases in far SOL but negligible heat flux on outer target
Ion convective energy transport implies inner divertor D_α should be later than outer divertor, delay should increase with density	Delays of D_α on same flux surface between inner and outer divertors	Delay smaller than predicted	**Absolute delay and density dependence consistent with predictions**
Ion convective energy transport implies inner divertor P_{rad} should be later than outer divertor, delay should increase with density	Delays of P_{rad} between inner and outer divertors	Inner divertor P_{rad} before outer divertor is inconsistent	**All delays consistent with simple model**

the ion convection time scale. This may be an indication of electron conduction effects [642,6653] consistent with the simple model. However, if electron energy conduction then raises the sheath potential at the targets, the model would predict that the temperature of the SOL should also rise and remain elevated for the order of an ion convection time. Since no such temperature rise is measured this may be an indication of local divertor target effects preventing a large rise in the sheath potential.

The broad radial effect of ELMs on the density in the outer midplane SOL seems inconsistent with the observation that the width of the ELM divertor heat flux was within a factor of 2 of the width between ELMs. For the flux expansion used in these discharges, the $\Delta R_{mid} = R - R_{sep} = 4.5$ and 6.5 cm surfaces at the midplane, corresponding to the

outermost measurements by Thomson scattering (Fig. 6) and reflectometry (Fig. 7), map to $\Delta R_{divo} = R - R_{OSP} = 22.4$ and 30.4 cm, respectively, from the OSP. Large increases in midplane SOL density were seen at both these radii as described above. The full width of the high heat flux region in the outer divertor is approximately 11 cm for the low and moderate density cases (Fig. 16). This is at least a factor of 2 less than would be expected from mapping of the upstream density perturbation profile. The baffle in the upper divertor intercepts flux surfaces with $\Delta R_{mid} > 4.8$ cm in the low density case and $\Delta R_{mid} > 3.8$ cm in the high density case so heat flux on the inner target, from ELMs at the outer midplane, would not be expected farther than $\Delta R_{divi} = R - R_{ISP} = 12.3$ and 9 cm respectively from the ISP. The heat flux profiles at the inner divertor have a full widths of only $\Delta R_{divi} = 7$ cm in the low density case and 5 cm in the high density case, so they are also a factor of 1.5 - 2 narrower than implied by the upstream density perturbation. These observations suggest that a fraction of the ELM power was deposited to the main chamber walls prior to transport to the divertors.

The rapid response of midplane recycling (D_α) to the ELM crash, especially in the low density case, is consistent with a local neutral source during the ELM from recycling of expelled ions at the main chamber surfaces. The D_α emission at the outer midplane rises rapidly with a time constant of ~100 μs at the time of the ELM thermal energy loss in the low density case (Fig. 9). This rise time is comparable to the perpendicular transit time from the pedestal to the main chamber limiter implied by the radial velocity in Fig. 8. It is substantially shorter than the time required for ion parallel transport to the targets, recycling there and neutral transport back up to the midplane. In addition, the data indicate that either poloidal or toroidal asymmetries exist in the refueling of the pedestal density. So, consistent with the measurements showing substantial density increase in the far SOL at low density, the D_α emission implies that a local recycling source may exist near the outer midplane during the ELM crash.

In the lowest density case ($n_e/n_{Gr} \sim 0.35$), the very small delay between ELM signatures on the D_α detectors in the inner and outer divertors indicates that mechanisms other than ion convective transport along field lines are playing a role in the divertor response to ELMs. The data at each density in Fig. 17 are from the chords that view the far SOL region of the target surface. The D_α signal increased in response to the ELM at all densities so the far SOL was attached to the targets. However, near the OSP the D_α emission during an ELM increased at moderate density ($n_e/n_{Gr} \sim 0.45$) but it decreased at high density ($n_e/n_{Gr} \geq 0.7$). No substantial change in the normalized delay on the outer flux surfaces was seen in this density range, even with this qualitative change in local strikepoint conditions. So local divertor detachment conditions may not be the explanation for the change in delay at the lowest density ($n_e/n_{Gr} \sim 0.35$). Finally, at moderate density a comparison of the far SOL D_α chords with two adjacent chords that

viewed the ISP and OSP respectively showed no delay between the chords viewing the outer divertor and no delay between the two chords viewing the strikepoints. The only observed delay was the ELM response far out in the SOL at the inner target compared with the other channels.

Several hypotheses exist that produce the correct functional dependence of these delays including 1) that the ELM density perturbation becomes vertically polarized in the SOL due to the ion B×∇B drift direction [79,80], and 2) that the nature of the ELM instability itself changes from ballooning dominated at high density to peeling dominated at low density. If the density perturbation remains toroidally localized as it propagates along SOL field lines, then the B×∇B drift polarization produces a particle drift away from (toward) the core plasma on the low (high) field side of the SOL that can broaden the footprint of the ELM on the outer target compared with the inner target footprint. If this broadening is comparable to the distance between the D_α chords in the two divertors, then the far SOL chord on the inner target might not respond to ELMs until after the perturbation recycles near the inner strikepoint and the associated neutrals migrate to the far SOL region near the target. This would introduce a delay of the far SOL response from the other chords. The difference in the size of the footprints decreases as the transit velocity to the targets increases so this would be consistent with the elimination of observed delay at low density and high parallel convection velocity. Another, very different explanation is that the ELM instability is more ballooning in character at moderate to high density and has the characteristics of an edge peeling mode at low density. The ballooning mode would be localized to the outer midplane consistent with the observed delays. The peeling mode could be localized around the X-point leading to little delay between observations in the divertors. This remains an area of active research.

In the low density case, the delay between observation of the ELM instability onset seen on the magnetics and the thermal energy loss at the ELM crash, indicated by the ECE and soft x-ray data, gives evidence for two phases of the ELM evolution. Similar observations have been reported on JT60-U and TCV [64,65]. The duration of the initial phase is ~500 μs in the low density case shown in Fig. 9. D_α emission at the midplane and in the divertors, and ion saturation current at the targets, all increase during this phase but high time resolution measurements that depend strongly on pedestal thermal energy do not change. This suggests that the initial phase perturbs particle density without affecting energy density. At the end of this period the ELM instability reaches reconnection. According to the simple model, the 500 μs of ELM build-up in this case is sufficient time to establish a loss channel for removal of thermal energy and as a result the pedestal temperature drops rapidly (~100 μs) when the modes saturate.

Pre-ELM conditions of the divertor plasma affect the response of the divertor to ELMs, so the solution that mitigates the damaging effect of ELMs on target surfaces depends on both control of the divertor conditions and control of perturbation characteristics at the pedestal. In the low density case spectroscopic emission profiles show that the inner divertor plasma, at low T_e and high n_e near the strikepoint, re-heats in response to the ELM. At high density both divertor leg plasmas are at low T_e and high n_e between ELMs. The inner divertor does not re-heat in response to ELMs but spectroscopy of the outer divertor indicates re-heating there. In addition, interferometer measurements of outer leg n_e show a large, rapid increase for the low density case but a significant, albeit slower, decrease is seen at high density. The D_α emission from neutrals is consistent with the density response. Finally, preliminary calculations of energy density on the divertor tiles show large increases during ELMs at the inner strikepoint, independent of density, as expected. However, the energy density during ELMs at the outer target decreases from about a factor of 2 lower than at the inner target at low density to very low levels at high density. The simple model of ELM energy transport in the SOL does not, by itself, explain any of these observations. All are determined by the local conditions of the divertor plasma prior to the ELM perturbation.

VII. CONCLUSIONS AND FUTURE WORK NEEDED

The simple model of ELM transport in the SOL, presented above, asserts that the majority of the ELM particle and energy transport should be dominated by ion convection physics and associated time-scales. One implication of this model is that the deposition profile of ELM energy on the targets should be determined by a competition between SOL parallel propagation at ion speeds and perpendicular transport across the SOL width. The minimum radial velocity of cross-field transport that would significantly affect the deposition profiles is approximately $vr = \lambda_p C_s/L$, where λ_p is the radial scale length for power in the SOL between ELMs, C_s is the ion sound speed evaluated at the pedestal temperature, and L is the shortest parallel distance from the midplane to one of the target surfaces. For DIII-D, $\lambda_p \sim 1$ cm, $C_s \sim 150$ km/s at pedestal temperatures of ~500 eV in deuterium, and the parallel distance to the OSP from the outer midplane is ~10 m. Therefore the prediction is that radial velocities greater than ~200 m/s would substantially broaden the power deposition profile on the targets. In addition, the model proposes that the deposition time should be of the same order as the ion transit time to the targets; for DIII-D this time is approximately 100 μs. Finally, according to the model the ELM energy delivered to the targets may be limited if the duration of the ELM instability at the midplane is shorter than the ion transit time.

Substantial experimental data support the simple model (Table 1) including: 1) the increase in delay between the inner vs outer divertor response to ELMs as density (and ion transit time) increases, 2) the observation that the thermal energy is not lost from the pedestal until after the instability has existed more than an ion transit time to the targets, and 3) the rise in the target density to values larger than the expelled density at the midplane. The theoretical prediction that the ELM perturbation is poloidally localized to the outer midplane is confirmed by the measurements in DN plasma shapes. The measured delays between ELM effects at the outer midplane and at the divertor targets are consistent with parallel propagation of pedestal temperature ions at the sound speed for the calculated field line lengths. In the intermediate and high density cases, the increase of the delays with increasing density between outer midplane and targets is consistent with the model. Also consistent is the increase with density of the delay between ELM effects at the outer target compared with the inner target. Finally, the observation of toroidal asymmetries in the net target surface currents is also consistent with the intermediate-n peeling/ballooning theory of the ELM instability and parallel propagation to the divertor.

Other measurements, including the dependence of pedestal thermal energy loss on operating density and the magnitude of the density rise at the outer target, indicate that some of the additional effects in the model may be playing a role. At high density the lack of temperature drop in the pedestal may indicate that the ion transit time to the targets is longer than the ELM instability duration so the energy can not be transported from the pedestal to the targets. Also pointing to this additional factor in the model is the observed delay between the pedestal particle loss and the thermal energy loss in the low density case. The delay is of the order of several ion transit times consistent with the picture that a channel must be established for energy loss to the targets before the pedestal energy drops. Of course, differences in the mode structure and drives for the ELM instability as functions of density [27,38,75] could also play a role in the evolution of the ELM cycle and must be included for a complete model. Finally, the fact that the density rise at the outer divertor far exceeds the density lost from the pedestal is an indication that release of deeply trapped neutrals in the surface, perhaps from bombardment by high energy ions falling through an elevated sheath [75], may be playing a role in the divertor response to ELMs.

A few of the observations from these experiments are completely inconsistent with the simple model including: 1) the relative delays of radiation pulse propagation at low density, and 2) the inconsistency between the narrow inner target heat flux vs the large increase in far SOL density at the midplane. At the lowest density ($n_e/n_{Gr} \sim 0.35$), the measurement of very small delay between ELM D_α jumps in the far SOL of the inner and outer target regions may indicate that local polarization of the ELM density perturbation is playing a role [79,80], or that the nature of the ELM instability changes qualitatively between low and high density. Electron conduction effects may be indicated by the relative delay of the radiation pulse in the inner compared with the outer divertor at low density. There are also inconsistencies at low density between large midplane density increase in the far SOL and the absence of large heat flux increase at the corresponding target locations especially in the inner divertor. At high density the very low target heat flux measured seems inconsistent with finite ion saturation current measured during ELMs. It is also inconsistent with the apparent re-heating indicated by the increase in CIII emission at the outer target during ELMs. Finally, the response of the outer divertor plasma at high density, in particular the reduction of D_α emission and density at the ELM, indicates that a cold dense divertor responds very differently to ELMs than ~~an~~ hot divertor. However, the response of the inner divertor, which is cold and dense at all but the lowest densities, is very different from the outer divertor response. Therefore, the pre-ELM density and temperature alone can not explain the outer divertor behavior. Clearly the local conditions near the targets can play a role that is as important in determining the loads on the targets as the differences in the source of particles and energy from the ELM instability at the midplane.

Future experimental work attempting to resolve the inconsistencies mentioned above should be focused primarily on achieving sufficient temporal resolution that physical conclusions can be obtained from multi-diagnostic analysis of individual ELMs; increased spatial resolution and comparisons between ELM effects for different ion B×∇B drift directions are also needed. A potentially serious flaw in the present state of ELM analysis in these and other experiments is that averaging or dataset merging of data from multiple ELMs must be done to get sufficient temporal information to draw conclusions about the underlying physics processes. The assumption is made that multiple identical ELMs can be made by holding steady conditions of control parameters in the experiments. However, ELMs by their very nature are highly nonlinear saturation of MHD instabilities and would not be expected to be reproducible. Therefore, full understanding of the physical processes driving parallel and perpendicular propagation of ELM energy and particles can only be obtained by analyzing one ELM event at a time. Statistics from those multiple results then should be compiled, rather than combining the raw data and analyzing the "average response." Improvements to the temporal resolution of ELM measurements are significantly easier that increasing the spatial resolution. However, the working model of ELM stability indicates that the modes have intermediate toroidal and poloidal mode numbers so there should be no expectation of toroidally or poloidally symmetric response in the SOL and divertor. It is also possible that the ELM structures in the SOL are rotating [61] further complicating the analysis from point measurements. Also the toroidally non-uniform SOL currents that result from the build-up to the ELM crash produce an effective dynamic error field that could feedback on the stability threshold in the pedestal and could affect the n-number of the mode that eventually goes to non-linear saturation [54]. The ability to predict the requirements for future divertor designs to be able to handle the anticipated ELMs will depend critically on having measurements and understanding of the toroidal peaking factors for ELM power and particle deposition on the targets. Duplication of fast ELM diagnostics at multiple toroidal locations and with finer radial resolution is therefore also essential in future experiments. All of these diagnostic improvements should be applied to detailed comparisons of ELM behavior as a function of density for both directions of the toroidal field to test the various theories based on collisionality and plasma drift effects.

Finally, significant advances are required in the computational modeling of the SOL and divertors to achieve predictive capability for ELM effects on target surfaces. Clearly from the data-model comparison presented above, future computations will need to include kinetic effects for both fast electron and fast ion populations, a highly collisional fluid-like background plasma, and plasma materials interactions physics (recycling and impurity generation) in a coupled time dependent computation. They will also need to include B×∇B, E×B, polarization and other drift effects. The required time scales for parallel transport physics alone range three orders of magnitude between fast electron and

neutral recycling physics so this is a challenging computational problem. Anomalous perpendicular transport, which may require a transport model for intermittent plasma objects, must also be included if the ion parallel convection times to the targets become comparable to the anomalous transport times to the main chamber walls. And the last component of a complete model needs to be a comprehensive nonlinear treatment of the ELM instability in the pedestal since this will produce the source term for the SOL/divertor simulation. Work to develop these computational tools is underway and the data presented above should provide a strong test of the models during the validation phase of this development.

REFERENCES

[1] PACHER H D (1996) E9. "Disruption and ELM Erosion, Appendix E9, Section 1.7 (Divertor)," ITER Design Description Document, ITER No. G 17 DDD 1 96-08-21 W2.1

[2] FEDERICI G *et al.* (2003)*J. Nucl. Mater.* **313-316**, 11

[3] LEONARD A W (1999) *J. Nucl. Mater.* **266-269**, 109

[4] LUXON J L, DAVIS L G (1985) *Fusion Tech.* **8**, 441

[5] GROEBNER R J (1993) *Phys Fluids B* **5**, 2343

[6] ZOHM H (1996) *Plasma Phys. and Contr. Fusion* **38**, 105

[7] SUTTROP W (2000) *Plasma Phys. and Contr. Fusion* **42**, A1

[8] CONNOR J W (1998) *Plasma Phys. and Contr. Fusion* **40**, 191

[9] LAO L L (2000) *Plasma Phys. and Contr. Fusion* **42**, A51

[10] SNYDER P B, WILSON H R (2002) *Contributions Plasma Physics* **42,** 258

[11] HUBBARD A E (2000) *Plasma Phys. and Contr. Fusion* **42**, A15

[12] HATAE T *et al.* (2001) *Nucl. Fusion* **41**, 285

[13] OSBORNE T H *et al.* (1999) *J. Nucl. Mater.* **266-269**, 131

[14] GROEBNER R J, OSBORNE T H (1998) *Phys. Plasmas* **5**, 1800

[15] MANICKAM J (1992) *Phys. Fluids B* **4**, 1901

[16] SAARELMA S *et al.* (1999) *Proc. 26th European Physical Society Conference on Controlled Fusion and Plasma Physics, Maastricht, The Netherlands* (European Physical Society, Petit-Lancy 1999) 1637

[17] HUYSMANS G T A *et al.* (1995) *Proc. 22nd European Physical Society Conference on Controlled Fusion and Plasma Physics Bournemouth United Kingdom* (European Physical Society, Petit-Lancy 1995) Part I, 201

[18] STRAIT E J *et al.* (1993) *Proc. 20th European Physical Society Conference on Controlled Fusion and Plasma Physics, Lisbon, Portugal* (European Physical Society, Petit-Lancy 1993) Vol. 17C, Part I, 211

[19] FERRON J R *et al.* (1994) *Proc. 21st European Physical Society Conference on Controlled Fusion and Plasma Physics, Montpellier, France* (European Physical Society, Petit-Lancy 1994) Vol. 18B, Part I, 86

[20] GOHIL P *et al.* (1988) *Phys. Rev. Lett.* **61**, 1603

[21] KASS T *et al.* (1998) *Nucl. Fusion* **38**, 111

[22] OSBORNE T H *et al.* (2000) *Plasma Phys. and Contr. Fusion* **42**, A175

[23] FERRON J R *et al.* (2000) *Nucl. Fusion* **40**, 1411; Ferron J R *et al.* (2000) *Phys. Plasmas* **7**, 1976

[24] GREENE J M, CHANCE M S (1981) *Nucl. Fusion* **21**, 453

[25] MILLER R L, LIN-LIU Y R, OSBORNE T H, TAYLOR T S (1998) *Plasma Phys. and Control. Fusion* **40**, 753

[26] TURNBULL A D *et al.* (1999) *Phys. Plasmas* **6**, 1113

[27] SNYDER P B *et al.* (2002) *Phys. Plasmas* **9**, 2037

[28] CONNOR J W, HASTIE R J, WILSON H R, MILLER R I (1998) *Phys. Plasmas* **5**, 2687

[29] SNYDER P B *et al.* (2002) *IAEA Fusion Energy Conference, Lyon, France,* submitted to Nucl. Fusion

[30] WILSON H R and MILLER R L (1999) *Phys. Plasmas* **6**, 873

[31] WILSON H R and SNYDER P B. (2001) *Proc. 28th European Physical Society Conference on Controlled Fusion and Plasma Physics, Madeira, Portugal* (European Physical Society, Petit-Lancy 2001)

[32] WILSON H R, CONNOR J W, FIELD A R *et al.* (1999) *Phys. Plasmas* **6**, 1925

[33] MERCIER C (1960) *Nucl. Fusion* **1**, 47; MERCIER C (1962) *Nucl. Fusion Suppl.* **2**, 801

[34] WILSON H R, SNYDER P B, HUYSMANS G T A, MILLER R L (2002) *Phys. Plasmas* **9**, 1277

[35] MOSSESSIAN D *et al.* (2002) *Plasma Phys. and Contr. Fusion* **44**, 423

[36] SNYDER P B and WILSON H R, (2003) submitted to *Plasma Phys. and Contr. Fusion* (this issue)

[37] THOMAS D M (2002) "Poloidal Magnetic Field Measurements and Analysis With the DIII-D Li Beam System," *Rev. Sci. Instrum* **74**, 154

[38] LEONARD A W *et al.* (2003) Phys. Plasmas **10**, 1765

[39] LAO L L *et al.* (1990) *Nucl. Fusion* **30**, 1035

[40] BERGMANN A (2002) *Nucl. Fusion* **42**, 1162

[41] TSKHAKAYA D (2002) *9th EU-TTF Workshop, Cordoba, Spain*, Paper O.I.13, submitted to Plas Phys Control Fusion (this issue)

[42] ROGNLIEN T *et al.* (2003) *J. Nucl. Mater.* **313-316**, 1000

[43] COSTER D P *et al.* (1997) J. Nucl. Mater. **241-243**, 690

[44] SOLANO E *et al.* (2002) *IEA Workshop on ELMs* (IEA Large Tokamak Collaboration) JET Facility Culham Science Center Abingdon OXON OX14 3DB United Kingdom

[45] OSBORNE T private communication.

[46] ZENG L *et al.* (2001) *Rev. Sci. Instrum* **72**, 320; ZENG L *et al.* (2003) *Rev. Sci. Instrum.* **74**, 1530

[47] BOEDO J A *et al.* (1998) *Rev. Sci. Instrum.* **69**, 2663

[48] COLCHIN R J *et al.* (2003) "The Filterscope," *Rev. Sci. Instrum.* **74**, 2068

[49] GRAY D S, LUCKHARDT S C, KELLMAN A G, CHOUSAL L, GUNNER G (2003) "Time Resolved Radiated Power During Tokamak Disruptions and Spectral Averaging of AXUV Photodiode Response in DIII-D," to be published in *Rev. Sci. Instrum.*

[50] FENSTERMACHER M E (1997) *Rev. Sci. Instrum.* **68**, 974

[51] GROTH M (2003) *Rev. Sci. Instrum.* **74**, 2064

[52] WATKINS J G private communication

[53] COLCHIN R J *et al.* (2002) *Nucl. Fusion* **42**, 1134

[54] TAKAHASHI H (2003) "Current in scrape-off layer plasma in DIII-D tokamak," to be submitted to *Nucl. Fusion*; TAKAHASHI H (2003) "Observation of current in SOL plasma and possible roles played by associated error field in AT discharges in DIII-D tokamak," *30th European Physical Society Conf. On Controlled Fusion and Plasma Physics, St Petersburg, Russia,* to be published

[55] LASNIER C J, *et al. Nucl. Fusion* **38**, 1225; HILL D N, *et al.* (1988) *Rev. Sci. Instrum.* **59**, 1878

[56] GREENWALD M, TERRY J L, WOLFE S M *et al. Nucl. Fusion* **28** 2199

[57] PETRIE T W (2003) *Nucl. Fusion* to be published

[58] CHANKIN A V *et al.* (2003) *J. Nucl. Mater.* **313–316**, 828

[59] LOARTE A *et al.* (2002) *Nucl. Fusion* **42**, 733

[60] ZENG L *et al.* (2003) *Bull. Am. Phys. Soc.* **47**, 276

[61] BOEDO J A *et al.* (2003) *Nucl. Fusion*, to be published

[62] BOEDO J A *et al.* (2003) *J. Nucl. Mater.* **313–316**, 813

[63] RUDAKOV D L *et al.* (2002) *Plasma Phys. and Contr. Fusion* **44**, 717

[64] CHANKIN A V *et al.* (2002) *Nucl. Fusion* **42**, 733

[65] PITTS R *et al.* (2003) "ELM Driven Divertor Target Currents on TCV," submitted to Nuclear Fusion

[66] JACHMICH S *et al.* (2001) *Proc. 28th European Physical Society Conference on Controlled Fusion and Plasma Physics, Madeira, Portugal* (European Physical Society, Petit-Lancy 2001) Vol. **25A,** 1617

[67] LAUX M *et al.* (2001) *Proc. 28th European Physical Society Conference on Controlled Fusion and Plasma Physics, Madeira, Portugal* (European Physical Society, Petit-Lancy 2001) Vol. **25A,** 1625

[68] COLCHIN R J (2003) "Neutral Particle Fueling at the Midplane of DIII-D," *J. Nucl. Mater.* **313-316,** 609

[69] GROTH M (2003) *J. Nucl. Mater.* **313-316,** 1017

[70] FENSTERMACHER M E *et al.* (1997) *Phys. Plasmas* **4**, 1761

[71] PETRIE T W *et al.* (1992) *J. Nucl. Mater.* **196-198**, 848

[72] FENSTERMACHER M E (1999) *Plasma Phys. and Contr. Fusion* **41**, A345

[73] FENSTERMACHER M E (1999) *J. Nucl. Mater.* **266-269**, 348

[74] EVANS T E *et al.* (1995) *J. Nucl. Mater.* **220-222**, 235

[75] LEONARD A W *et al.* (2003) *J. Nucl. Mater.* **313-316**, 768

[76] HERMANN A (2003) *J. Nucl Mater.* **313-316**, in press

[77] HORTON L *et al.* (2001) *Proc. 9th European Fusion Physics Workshop, Saariselka, Finland*

[78] HERMANN A *et al.* (1995) *Plasma Phys. and Contr. Fusion* **37**, 17

[79] KRASHENINNIKOV S *et al.* (2001) *Phys. Rev. Lett. A* **283**. 368

[80] PETRIE T W *et al.* (2003) private communication

[81] ITER Physics Basis (1999) *Nucl. Fusion* **39**, 2137

ACKNOWLEDGMENTS

This work was supported by the U.S. Department of Energy under Contract Nos. W-7405-ENG-48, DE-AC03-99ER54463, DE-AC05-00OR22725, DE-AC02-76CH03073, DE-AC04-94AL85000, and Grant Nos. DE-FG03-95ER54294 and DE-FG03-01ER54615.